RESEARCH ARTICLE

WILEY

Experimental and numerical validation of guided wave phased arrays integrated within standard data acquisition systems for structural health monitoring

Wentao Wang[1,3] | Hui Zhang[2] | Jerome P. Lynch[1] | Carlos E.S. Cesnik[2] | Hui Li[3]

[1] Department of Civil and Environmental Engineering, University of Michigan, Ann Arbor, MI 48109, USA

[2] Department of Aerospace Engineering, University of Michigan, Ann Arbor, MI 48109, USA

[3] Key Lab of Structures Dynamic Behavior and Control of the Ministry of Education, Harbin Institute of Technology, Harbin 150090, China

Correspondence
Jerome P. Lynch, Department of Civil and Environmental Engineering, University of Michigan, Ann Arbor, MI 48109, USA.
Email: jerlynch@umich.edu

Summary
Phased array methods are a promising approach to damage detection by enabling guided wave steering and beam focusing leading to improved localization and sizing of structural damage. Due to the costs and challenges to addressing piezoelectric arrays in parallel, most phased array methods actuate piezoelectric elements one at a time in round-robin fashion with postprocessing algorithms used to synthetically steer and focus the guided waves. In this study, true parallel excitation and sensing of ceramic piezoelectric actuators is implemented in a standard structural health monitoring data acquisition system without requiring highly specialized and expensive ultrasonic data acquisition equipment. The study performs both numerical simulation and laboratory experiments to illustrate the damage detection capabilities of a piezoelectric phased array. Laboratory experiments are first performed using the high-speed data acquisition system to actuate and sense piezoelectric elements bonded in a linear array on an aluminum plate. To visualize the direction and focal point of the guided waves, a laser Doppler vibrometer triggered by the data acquisition system is adopted to scan the surface displacements of the plate. The study verifies that the location and size of damage can be accurately detected in the plate using the phased array operated by the structural health monitoring data acquisition system. To explore the capabilities of the system to detect different damage cases, the computationally efficient local interaction simulation approach is implemented on a graphic processing unit to simulate the performance of a linear phased array to steer and focus Lamb waves for damage detection.

KEYWORDS
damage detection, Lamb waves, phased array, structural health monitoring, ultrasonic

1 | INTRODUCTION

Structural health monitoring (SHM) is an emerging asset management tool that provides structural managers the means to quantitatively assess the health of structures. SHM can play an especially important role in ensuring structural safety while reducing asset lifecycle management costs in many engineering fields including in civil, naval, mechanical, and aerospace engineering.[1] The identification and characterization of damage and deterioration in large and complex

structures has proven to be an especially challenging problem for the SHM research community. For example, global approaches (such as those using accelerometers) have proven to be relatively insensitive to small levels of damage.[2,3] Similarly, strain-based approaches can also be insensitive to damage unless the strain measurement is taken in locations where damage affects strain fields.[4,5] To overcome these limitations, the SHM community is exploring the use of ultrasonic guided waves for damage detection.

Ultrasonic guided waves are elastic stress waves that propagate long distances within structural components that have surface boundaries. Ultrasonic guided waves introduced using piezoelectric actuators bonded to the surface of the structure have been intensely studied for damage detection in SHM because they are a repeatable investigative approach capable of interrogating large areas of a structure. The propagation, reflection, and scattering properties of guided waves using different excitation sources and damage types have previously been studied for a wide variety of structure types.[6] In particular, Lamb waves have been explored for damage detection in thin-walled structures such as metallic plates,[7] composite plates,[8,9] I-beams,[10] and pipelines.[11] Lamb waves can travel long distances with little attenuation allowing them to effectively interrogate a large area using a single transducer.[11,12] Lamb wave propagation has been previously studied using theoretical,[13,14] numerical,[7,15] and experimental[8,16] methods. Propagating Lamb waves measured using piezoelectric elements bounded to the surface of the structure can be analyzed to locate and characterize structural damage such as cracks, delamination, holes, and notches.[14,17] Damage detection in metallic and composite plates using Lamb waves has been proposed using various approaches including waveform,[18,19] time of flight,[20] time reversal,[8] and laser vibrometry[21] methods.

In general, the dispersive nature of Lamb waves can make interpretation of measured waveforms difficult. For example, dispersion of the multiple Lamb wave modes results in mode mixing that can obscure individual modes in a measured waveform. It can also be difficult to distinguish waveforms associated with boundary reflections from those associated with damage.[16] To overcome some of these challenges, phased array (PA) techniques can be used to focus and steer guided waves generated by piezoelectric elements to enhance damage localization and characterization.[12] Unlike methods that employ a single piezoelectric element, PA techniques rely on multiple piezoelectric elements assembled in linear or grid arrays. By manipulating the time delay between excitation signals emitted by each piezoelectric element, the PA can scan and focus the desired guided wave mode at a user-defined focal point in the structure. Specifically, varying the waveform phase and amplitude generated by each PA element results in constructive interference and the creation of a wave front with a desired direction and focal area.[22,23] The design of linear and grid PA setups have been reported in the SHM literature for the detection of damage in plates, pipes, and rails.[24–26]

The data acquisition hardware required to implement a PA aperture in a truly parallel fashion has historically been both costly to acquire and are designed to serve as stand-alone guided wave systems. The most widely reported parallel data acquisition system for PA-based SHM has been the Phased Array Monitoring for Enhanced Life Assessment system.[27] Although this system is reported to be capable of exciting and sensing up to 12 piezoelectric elements in a frequency range of 30 kHz to 1 MHz, the system is a prototype platform and not widely available. To lower the need for sophisticated data acquisition systems, the vast majority of PA approaches adopt a synthetic aperture strategy where piezoelectric elements in the PA are operated individually to pulse the structure in a round-robin fashion. Each waveform generated by a single piezoelectric element has a spherical wave front in a thin plate; upon encountering damage, the wave is partially reflected back toward the piezoelectric array. A beamforming algorithm of delay and sum is then applied as a signal processing approach to identify the location of damage that produces wave scattering and reflections. Although a synthetic PA approach is cost-effective, it does not reap the full benefits of the PA, which has the ability to focus the PA waveform energy on specific locations in the plate structure. For high attenuative media (e.g., composite materials), the synthetic PA will have a lower signal-to-noise ratio (SNR) than a true PA approach. Furthermore, synthetic PA strategies are slower due to the need to excite the array in round-robin fashion and postprocessing. In contrast, parallel PA operation offers much faster inspection capabilities due to a quicker approach to data acquisition and reduced postprocessing demands. A summary of the major differences between synthetic and true parallel excitation PA approaches are presented in Table 1.[24]

To gain the full benefits of a guided wave PA in SHM, true parallel excitation and sensing of piezoelectric arrays are desired in a cost-effective and easy to use data acquisition system. Furthermore, recent summary reviews of the guided wave SHM field have emphasized the need to combine guided wave methods with more traditional SHM approaches (such as those using accelerometers and strain gages) within the same data acquisition architecture.[28] Hence, this study aims to develop a PA data acquisition system capable of high-speed parallel excitation and sensing of PA elements using a standard data acquisition platform widely used in SHM applications; in doing so, the study will offer a versatile SHM system capable of both guided wave and traditional SHM data collection methods. The study focuses on the design and

TABLE 1 Key differences between synthetic and parallel excitation phased array approaches

	Synthetic PA	Parallel excitation PA
Excitation	Excited by *1* piezoelectric element	Excited by *N* elements
Sensing	Received by *N-1* piezoelectric elements	Received by *N* elements
Excitation sequence	One by one in round robin fashion	Simultaneously with different time delays
Time delay	No time delay	Variable time delays
Focusing	Physical focusing not possible	True physical focusing
Focal point	No	Yes
Processing	Postprocessing	Preprocessing and postprocessing
Signal-noise ratio	Moderate	High
Wave field	Spherical wave (i.e., cylindrical waves in thin plate)	Focused wave beam
Wave mode	Both S_0 and A_0	A_0 mode
Detection	Steering by postprocessing mathematics	Steering and focusing in the physical domain with high signal-noise ratios

Note. PA = phased array.

implementation of a multichannel National Instruments data acquisition system capable of exciting and sensing linear piezoelectric arrays bounded to the surface of the structure. The system is designed to actuate each channel in the PA with highly precise time delays to form directional beams that focus on a programmable point in the structure. The study also develops an imaging method in LabVIEW that allows system end users to spatially observe the location and size of damage in the structure using the PA system. The study utilizes a PA of seven elements bounded to the surface of a large aluminum plate for experimental validation of the system. Another novelty of the study is the integration of a laser Doppler vibrometer (LDV) within the National Instruments system to verify the existence of focused waveforms generated by the PA. Finally, the work adopts the local interaction simulation approach (LISA) that is executed on a graphical processing unit to numerically simulate waveforms in the experimental setup with high simulation speeds. LISA modeling provides a means of validating the PA and LDV data acquired by the integrated National Instruments data acquisition system and the opportunity to consider different PA designs and detection capabilities for more realistic damage cases.

2 | INTEGRATED DATA ACQUISITION SYSTEM FOR GUIDED WAVE SHM

If guided wave methods are to be adopted in practical SHM deployments, the cost and complexity of their data acquisition systems must be low. Structural owners would avoid the adoption of multiple data acquisition platforms in their structures and would seek one system with multiple capabilities. In this study, a single SHM data acquisition architecture is proposed for both guided wave inspection and traditional SHM data collection from sensors such as strain gages and accelerometers. A commonly used National Instruments data acquisition is adopted and expanded to include the capability for PA-based guided wave inspection of structures.

A National Instruments PXIe-1082 chassis is adopted capable of the installation of multiple data acquisition cards. In this study, emphasis is placed on the selection of data acquisition cards capable of offering high-speed input and output sampling in the ultrasonic regime. Four data acquisition cards (PXIe-6361, PXIe-6124, and two PXI-6115) are installed in the PXIe-1082 chassis to both excite and record data from PZT elements bonded to the surface of a structure. The number of channels and sampling rates vary for the different data acquisition cards. The PXIe-6361 is capable of two analog output channels and 16 analog input channels; the analog inputs are sampled with a 16-bit resolution and with a maximum sampling rate of 2 MHz. The PXIe-6124 has two analog output channels and four analog input channels; the analog inputs are sampled with a 16-bit resolution and with a maximum sampling rate of 4 MHz. Finally, the PXI-6115 has 2 analog output channels and four analog input channels; the analog inputs are sampled with a 12-bit resolution and with a maximum sampling rate of 10 MHz. This experimental setup provides versatility to the SHM system designer in that it offers multiple input and output channels capable of high sampling rates.

LabVIEW is used to create a user interface to the National Instruments data acquisition system. Graphical user interfaces that allow end users to collect data from the channels and visualization of the data collected is offered. Also, the

LabVIEW platform is used to process the waveforms selected to convert ultrasonic waves into information specific to damage in the monitored structure. In this study, LabVIEW is used to address the PA piezoelectric elements with waveforms selected by the end user. It will be used to calculate time delays between the PA channels to steer the waveform to desired PA focal points. Finally, waveforms collected will be used to image damage location and severity in polar plots.

3 | ULTRASONIC PA METHOD

3.1 | Lamb waves in plates

Lamb waves are elastic stress waves generated in thin-walled structures that have two, traction free boundaries. Due to the two surfaces, an infinite number of guided wave modes can be excited in the thin plate. Guided wave modes in a thin plate are of two types: symmetric (S_i) modes whose particle displacements are symmetric about the midplane ($z = 0$) and asymmetric (A_i) modes whose particle displacements are antisymmetric about the midplane. The subscript i on both mode types designates the mode number as shown in Figure 1. The phase, c_p, and group, c_g, velocities of Lamb waves vary with the signal frequency, f, times the thickness of the plate, d, as shown in Figure 2 for an aluminum plate. Lamb waves are highly efficient and can propagate over relatively long distances without significant attenuation of their waveforms.[16] This particular property is attractive for SHM because it allows guided wave transducers to interrogate large areas of a structure for damage.

The characteristic (Rayleigh–Lamb) equations for thin plates with traction free surfaces are[12]

$$\frac{\tan \beta h}{\tan \alpha h} = \left[\frac{-4\alpha\beta k^2}{(k^2 - \beta^2)^2} \right]^{\pm 1} \tag{1}$$

as derived from sinusoidal solutions to the wave equation with the traction free plate surfaces as boundary conditions. The sign of the exponent in Equation 1 corresponds to the mode type (+1 for symmetric modes, S_i, and −1 for antisymmetric modes, A_i), k is the wave number, and h is the half thickness of the plate. Furthermore, α^2 and β^2 are defined as

$$\alpha^2 = \frac{\omega^2}{c_l^2} - k^2 \tag{2}$$

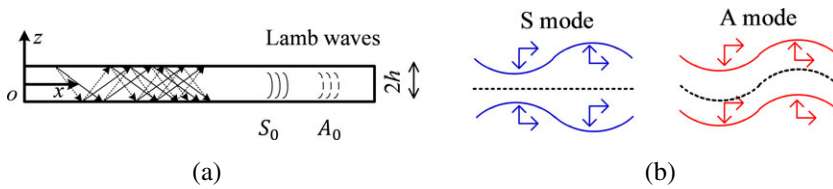$$\beta^2 = \frac{\omega^2}{c_s^2} - k^2, \tag{3}$$

FIGURE 1 (a) Lamb waves in a thin plate of thickness 2 h; (b) motion of body media in symmetric (S) mode and antisymmetric (A) modes
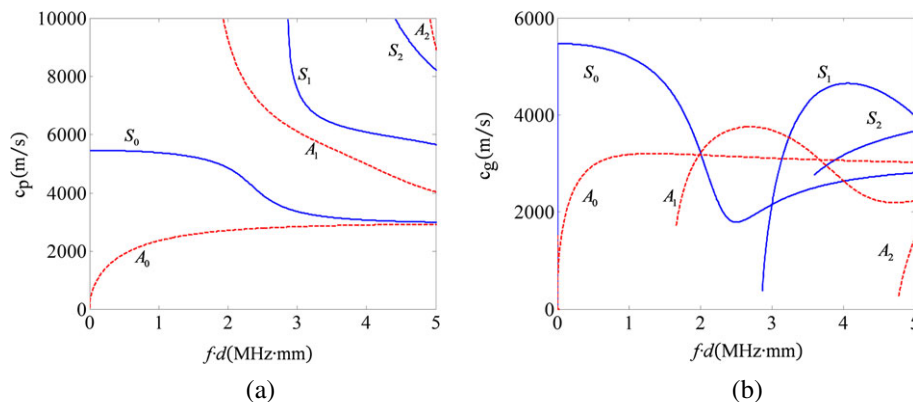

FIGURE 2 Dispersion curves of Lamb waves in an aluminum plate: (a) phase velocity, c_p, and (b) group velocity, c_g, of multiple wave modes

where c_l is the velocity of pressure (longitudinal) waves, c_s is the velocity of shear waves in the plate material (which are functions of the material Young's modulus E and Poisson's ratio ν), and ω is angular frequency. For real wave numbers ($k \in \mathbb{R}$, which correspond to undamped waves in the plate), Equation 1 can be solved numerically to find the frequency, ω, and Lamb wave mode phase velocity $c_p = \omega/k$. The group velocity is defined as $c_g = d\omega/dk$ and can be written in terms of c_p,[12]

$$c_g = c_p{}^2 \left(c_p - f \cdot d \frac{dc_p}{d(f \cdot d)} \right)^{-1},$$

(4)

where $f = \omega/(2\pi)$ and $d = 2h$. The c_p and c_g values derived for each frequency can be plotted as a function of $f \cdot d$ resulting in the dispersion curves of Lamb waves in a plate of thickness d. The dispersion curves of a 6061aluminum plate are presented in Figure 2. For example, in a 1.6-mm-thick 6061 aluminum plate, a 100-kHz Lamb wave has two modes, namely, the S_0 and A_0 modes with phase velocities of 5,465 and 2,172 m/s, respectively.

3.2 | PA principles

PA techniques for ultrasonic waves in solid media have evolved from the concept of scanning antenna arrays used in radar systems. Today, ultrasonic PA techniques are widely used in the medical (for the imaging of tissue and organs inside the body) and nondestructive evaluation (to identify damage and flaws within structures) fields.[22,24] In the field of SHM, there is wide interest in using PA techniques to improve the damage detection capabilities of SHM systems. The ultrasonic guided wave PA consists of an ordered array of piezoelectric elements bounded to the structure in a linear, grid, or circular array pattern. In an active array, each array element can be individually excited with any waveform desired. Most PA systems apply waveforms precalculated to ensure the waves generated by each element constructively interfere in the physical domain to develop a directional ultrasonic wave focused on a specific structural area. Waves focused on the damaged region will reflect and scatter; these reflected waves are acquired by the PA. By adjusting the beam direction and focal length of the PA, the structure can be scanned by the SHM system to find areas of damage. In this study, a true active PA system will be presented consisting of N piezoelectric lead zirconate titanate (PZT) elements configured as a linear PA. All N piezoelectric elements are addressable for both actuation and sensing. The PA elements will be excited individually with phase shifts introduced between array elements to develop a steerable waveform at a desired focal length. This approach is in contrast to previously proposed piezoelectric-based PA methods that rely on synthetic aperture approaches implemented in postprocessing.[24] By truly focusing the wave beam in the physical domain, the advantage of a higher SNR in the received waveforms will be gained, which improve the damage localization and characterization capabilities of the system.

3.3 | PA focusing

A hypothetical linear PA consisting of nine PZT elements excited and sensed by a multichannel data acquisition system is shown in Figure 3a. Each element is indexed by the variable n while the distance between the center line of each element is constant at a. By applying the same, but time-delayed waveform to each element of the linear PA, a controllable wave front can be generated through superposition of the individual waves generated by each element of the PA. For example, the PZT element at the top ($n = 1$) is excited first and emits a circular wave front that spreads out with a radius r_1 that grows linearly with time. The second topmost PZT ($n = 2$) is excited next and emits the same wave. The process continues down the line until all the PZTs have been excited. Through superposition, the individual waveforms sum to form a wave front with directionality θ_F (relative to the center of the PA) concentrating on a focal point P. The focal point is at a radius R_F from the center of the PA. By adjusting the time delays between the PZT elements in the PA, both the angle of the directional wave front and the focal point can be varied. This allows the PA to scan specific areas of a structure for damage. If damage is present in the structure at focal point, P, wave fronts will be backscattered with a high SNR. If damage is located elsewhere (i.e., not at P), the backscattered waveforms received by the PA will be weak with low SNRs. For the case where damage is present at the focal point, the backscattered wave energy is equivalent to a wave energy point source at P. To spatially image the damage, the signals received by each PZT element are shifted based on the original time delay and superimposed to derive a reconstructed signal. If there is a defect at the focal point, the superimposed signal received by the PA will have a significant amplitude.
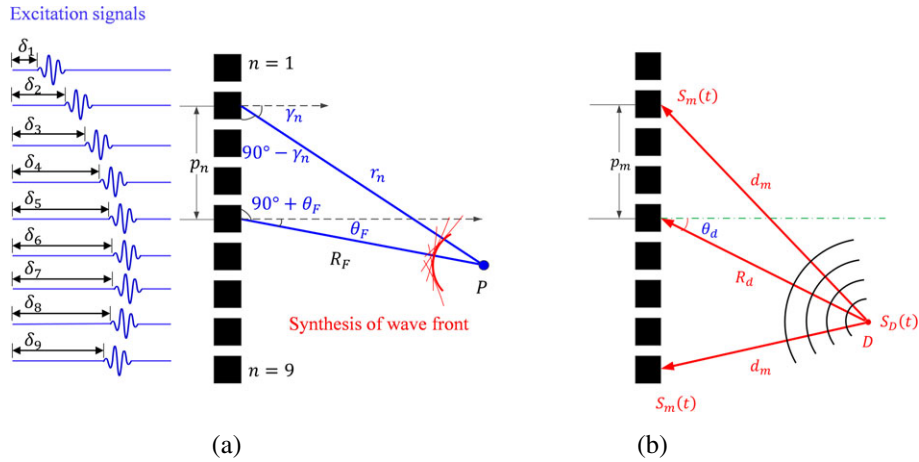
FIGURE 3 Geometry of a nine-element linear phased array: (a) directional steering to a focal point P; (b) backscattered wave from damage at D

Lamb waves have at least two modes at each frequency with each mode having a group velocity and amplitude. To maximize the SNR of the received backscattered signal from damage at P, the mode with the largest wave amplitude should be explicitly considered. To derive the amplitude tuning curves of the A_0 and S_0 modes in a 1.6-mm-thick 6061 aluminum plate using a 100-kHz three-cycle tone-burst signal, the method delineated by Giurgiutiu[14] is used. The normalized amplitude of the A_0 mode is greatest as shown in Figure 4.

When determining the time delay associated with each PZT element, δ_n, two parameters are considered: the group velocity of the A_0 mode and the radial distance from the element to the focal point, r_n. At a center frequency of 100 kHz, the group velocity of the A_0 mode based on the dispersion curves of Figure 2b is $c_g = 2172$ m/s. The radial distance from the nth PZT element in the PA to the focal point P is r_n. This distance can be shown to be equal to

$$r_n = \sqrt{(p_n)^2 + R_F{}^2 - 2R_F \cdot (p_n)\sin(\theta_F)}, \qquad (5)$$

where p_n is the distance from the center line of the PA to the nth PZT element and R_F is the distance from the center of the PA to the focal point, P. To ensure that the waveforms arrive at P at the same time, the time delay for the nth element can be calculated by dividing the distance to the focal point, r_n, by the group velocity, c_g,

$$\delta_n = t_0 + \frac{R_F}{c_g} - \frac{R_F}{c_g}\sqrt{1 + \left(\frac{p_n}{R_F}\right)^2 - 2\frac{p_n}{R_F}\sin\theta_F}, \qquad (6)$$

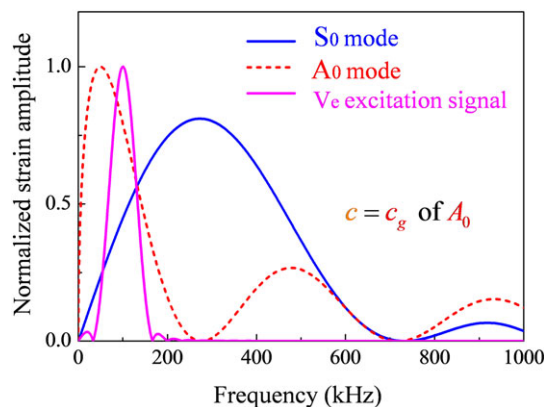where the term t_0 is a constant to ensure that δ_n is never a negative value.[29]

FIGURE 4 Normalized strain amplitude for three-cycle 100-kHz tone burst enclosed in a Hanning window in a 1.6-mm-thick 6061 aluminum plate

The amplitude of the waveform will attenuate as a function of $\sqrt{r_n}$. Hence, the summation of wave amplitudes (i.e., acoustic pressure, S_p) at the focal point is

$$S_p(t) = \sum_{n=1}^{N} \frac{A_n}{\sqrt{r_n}} \cdot S_0\left(t - \frac{r_n}{c_g} - \delta_n\right), \tag{7}$$

where N was previously defined as the total number of elements in the array, S_0 corresponds to the base waveform shifted in time to account for the waveform travel time, and A_n is a scalar factor adjusting the waveform amplitude for the nth PA element.

3.4 | Damage imaging

Assume damage exists in the structure at a site D with distance R_d and angle θ_d from the center of the PA as shown in Figure 3b. To find this damage state, the PA is commanded to sweep the azimuth with increasing focal length R_F. If there is damage at azimuth θ_d and distance R_d, the sweeping ultrasonic beam will form a strong backscatter echo with a high SNR as previously described. The wave amplitude launched by the active PA focusing on the damaged site is represented by a modification of Equation 7:

$$S_D(t) = \sum_{n=1}^{N} \frac{A_n}{\sqrt{d_n}} \cdot S_0\left(t - \frac{d_n}{c_g} - \delta_n\right), \tag{8}$$

where the distance from the nth PA element to the damage site, D, is

$$d_n = \sqrt{(p_n)^2 + R_d^2 - 2R_d \cdot (p_n)\sin(\theta_d)}. \tag{9}$$

At the damaged site, it is assumed that the signal is reflected with backscatter coefficient $B \in (0, 1]$. Thus, considering the round trip of each ultrasonic wave originated by the individual PA elements, the signal received by the mth element of the passive PA will be $(B/\sqrt{d_m}) \cdot S_D(t - d_m/c_g)$, as shown:

$$S_m(t) = \sum_{n=1}^{N} \frac{B}{\sqrt{d_m}} \cdot \frac{A_n}{\sqrt{d_n}} \cdot S_0\left(t - \frac{d_n + d_m}{c_g} - \delta_n\right), \tag{10}$$

where

$$d_m = \sqrt{(p_m)^2 + R_d^2 - 2R_d \cdot (p_m)\sin(\theta_d)}. \tag{11}$$

The passive PA assembles the signals received by all of the piezoelectric elements and superimposes them with the appropriate delays to yield S_R:

$$S_R(t) = \sum_{m=1}^{N} S_m(t - \delta_m), \tag{12}$$

where the appropriate time delay, δ_m, is

$$\delta_m = t_0 + \frac{R_D}{c_g} - \frac{R_D}{c_g}\sqrt{1 + \left(\frac{p_m}{R_D}\right)^2 - 2\frac{p_m}{R_D}\sin\theta_D}. \tag{13}$$

If a structure is an ideal plate with infinite boundaries and no damage, the PA will not receive a backscattered signal. Hence, if $S_R > 0$ is received, it indicates that damage is present at θ_d and R_d. Furthermore, if there is a damage at the focal point, the energy of the superimposed difference signal will have a significant magnitude that is easy to detect.

4 | LABORATORY EXPERIMENTATION

4.1 | Experimental setup

To evaluate the proposed PA methodology, a thin plate structure in which damage is introduced is adopted for experimental validation. The structure is a thin aluminum alloy 6061 plate 91.4 cm by 91.4 cm in area with a thickness of 1.6 mm. The material properties of 6061 aluminum are Young's modulus, E, of 69.0 GPa, Poisson's ratio, ν, of 0.33, and density, ρ, of 2,700 kg/m^3. In the center of the plate, a linear PA consisting of seven d_{31}-type PZT elements (Piezo Systems PSI-5A4E) 0.508 mm thick with nickel-plated surfaces are attached to the top surface of the plate. The PZT elements are cut to be 7 mm by 7 mm in area using a wafer dicing saw. The elements are bonded to the aluminum plate using standard cyanoacrylate glue in a linear array with elements 1 mm apart. Wires that establish a connection between the PZT elements and a laboratory data acquisition system are bonded to the top surface of each element using copper tape. This PA is considered both the active and passive PA and will be used to generate ultrasonic guided waves and measure the waveforms in the plate.

To collect data, two data acquisition systems are used: the aforementioned National Instruments data acquisition system and an LDV. To command the seven elements of the PA using the National Instruments system, the two analog output channels of all four data acquisition cards (PXIe-6361, PXIe-6124, and two PXI-6115) are utilized with one of the output channels reserved to trigger the LDV system. The seven PZT elements of the PA are collected using seven channels of the PXIe-6361 data acquisition card. LabVIEW is used to create a user interface to the National Instruments data acquisition system with the user capable of commanding the PA to attain any desired focal point using an excitation waveform. LabVIEW ensures time synchronization between all of the input and output channels irrespective of which data acquisition card is generating or measuring signals. During data acquisition, LabVIEW commands the generation and measures the signals in the PA with a sampling rate of 1 MHz for each element. In order to eliminate the effect of plate vibrations on the received signals, a Chebyshev I band-pass filter with a passband from 20 to 500 kHz is applied by postprocessing in LabVIEW.

The second data acquisition system consists of a scanning Polytec PSV-400 LDV that can measure the out-of-plane velocity of a structure at discrete points over a defined area. The LDV is setup in the laboratory (Figure 5) roughly 1.0 m from the plate with the laser oriented orthogonal to the plate surface. In this study, an area roughly 28.6 cm by 36.6 cm to the left of the linear PA is measured using the LDV. The PSV-400 is programmed to collect data at 22,400 measuring points defined over a 140 by 160 grid array. To enhance the measurements taken by the LDV, a retroreflective sheet is attached to the plate in the area the LDV will scan. One output channel from the National Instruments data acquisition system is used to trigger the PSV-400 to ensure both data acquisition systems are time synchronized. To image the full wave field, the LDV is set up to measure the out-of-plane velocity time history at each measurement point. The PA is commanded to introduce ultrasonic guided waves into the plate using an identical excitation set for each LDV measurement point. Given the large number of measurement points in the plate, 22,400 PA excitations are applied. At each point, the excitation is applied 20 times with signals averaged to remove measurement noise.

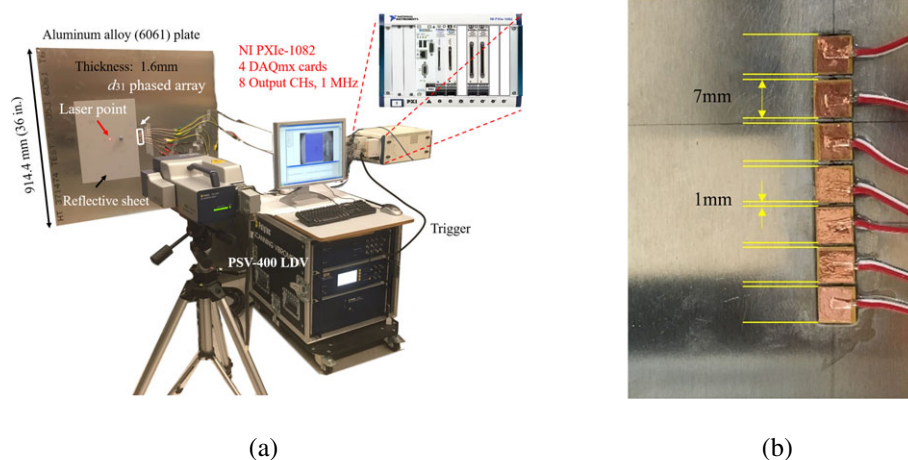(a)   (b)

FIGURE 5   (a) Aluminum plate (with linear phased array installed) and the laser Doppler vibrometer (LDV) instrument in the laboratory; (b) close-up view of phased array PZT elements ($n = 7$)

4.2 | Wave field in pristine plate

To observe the beam steering capabilities of the PA using the LDV system, the plate in a pristine (undamaged) condition is excited with the PA configured to achieve three focal points at (a) $R_F = 10.0$ cm and $\theta_F = 0°$, (b) $R_F = 10.0$ cm and $\theta_F = 30°$, and (c) $R_F = 10.0$ cm and $\theta_F = 45°$. A three-cycle sinusoid tone-burst signal enclosed in a Hanning window is chosen as the basic excitation signal as shown in Figure 6 in both the time and frequency domains. The center frequency of the signal is selected to be 100 kHz to excite the A_0 and S_0 modes and to ensure that the modes are separable due to differences in their group velocities (Figure 2b). As a result of their differing group velocities, the two modes will be easier to distinguish from the backscattered waves generated by damage. The voltage amplitude of the waveform is set to 5 V. Using the three-cycle tone burst, LabVIEW calculates the time delay between the PZT elements of the PA to achieve the desired focal points. For example, to achieve the first case ($R_F = 10.0$ cm and $\theta_F = 0°$), the time delay between adjacent PZT elements in the array are 0, 0.722, 1.160, 1.307, 1.160, 0.722, and 0 μs. To achieve the second case ($R_F = 10.0$ cm and $\theta_F = 30°$), the time delay between adjacent PZT elements in the array are 10.815, 9.611, 8.132, 6.405, 4.458, 2.315, and 0 μs. The LDV system is used to image the wave field in the plate as a function of time.

Figure 7a shows the out-of-plane wave field of the PA in the plate at three instances in time. The wave field is clearly directional with the prescribed angle of $\theta_F = 0°$ with energy concentrating 10 cm from the PA. As the wave field continues past the focal point, it disperses before encountering the plate boundary. The out-of-plane displacement wave fields are all summed as presented to the far right of Figure 7a; the summed wave fields clearly show the directionality of the wave field and the focal point at 10.0 cm. Figure 7b and 7c is similar with the wave field achieving the desired directional angle of $\theta_F = 30°$ and $\theta_F = 45°$, respectively. There are two additional features in Figure 7c worth mentioning. First, a side lobe is seen roughly 90° from the main lobe wave field. Due to the interaction of the wave fields from the individual PZT elements, side lobes will be generated but the main lobe dominates. The second feature is the sensitivity of the wave fields to minor defects in the pristine such as a small scratch as denoted in Figure 7c.

4.3 | Wave field in damaged plate

The behavior of the wave field in the presence of damage is of interest. To simulate damage in the aluminum plate, two identical magnets 1.27 cm by 1.27 cm in size are attached to each side of the plate at the same location. The advantage of using magnets to simulate damage is the ability to move them to any desired location without permanently altering the plate. The magnets are placed at $R_d = 10.0$ cm and $\theta_d = 5°$. Similar to the pristine plate, the PA is programmed to focus on $R_F = 10.0$ cm at $\theta_F = 0°$, $\theta_F = 30°$, and $\theta_F = 45°$. Figure 8a provides a plot of the wave field at three instances in time identical to that of Figure 7a. However, evident in Figure 8a is the interaction between the wave field and the magnets with the magnets generating a strong backscattered wave field that can be acquired by the PA. When the beam is steered to $\theta_F = 30°$, the interaction between the magnets and the wave field is minimal with little back scattered energy being reflected back to the PA. The same occurs for $\theta_F = 45°$ as shown in Figure 8c.
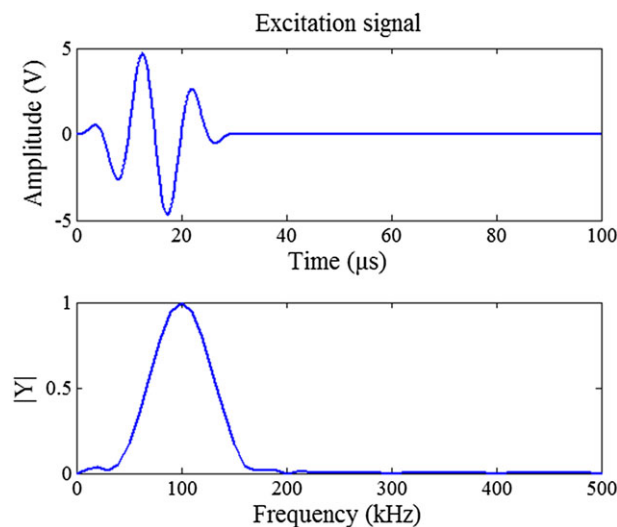

FIGURE 6 Basic tone-burst signal in the time (top) and frequency (bottom) domains
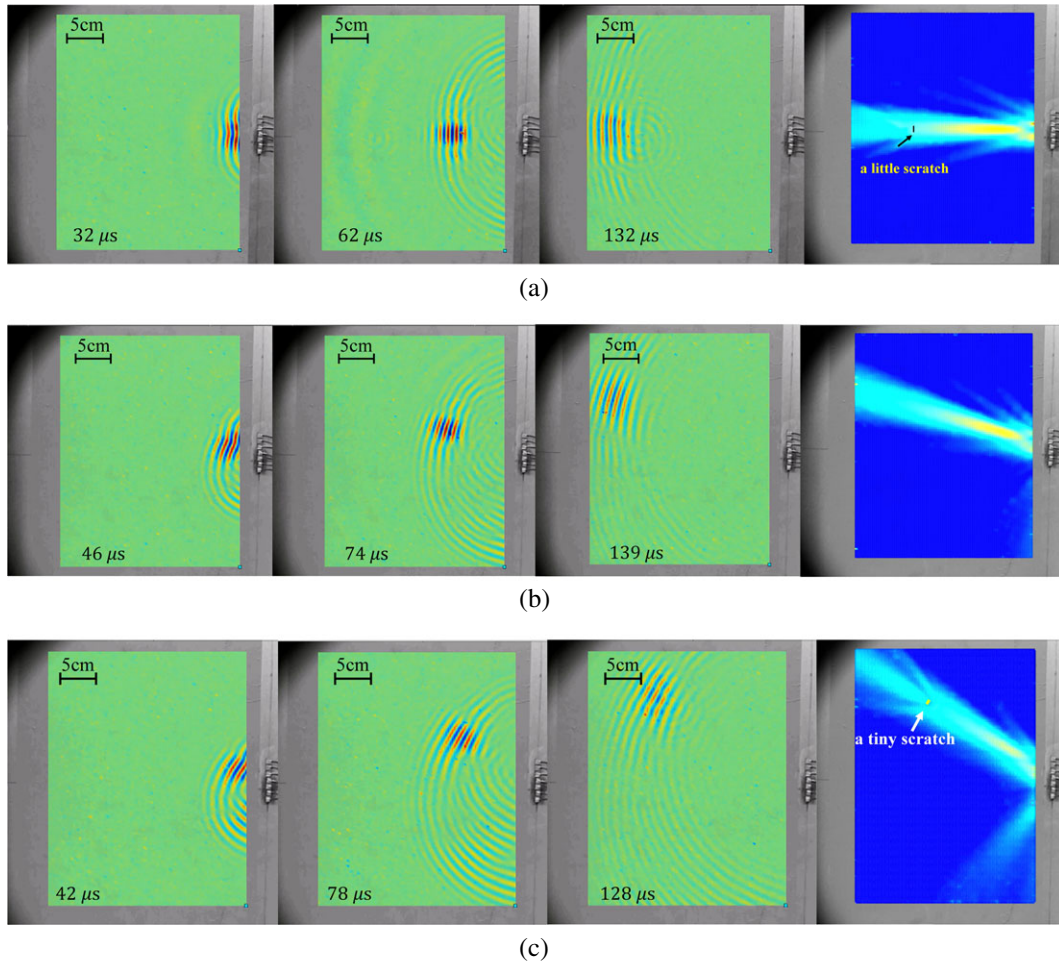
(a)

(b)

(c)

FIGURE 7 Wave field in undamaged aluminum plate measured by laser Doppler vibrometer when the focal point is $R_F = 10$ cm and at a beam angle, θ_F, of (a) 0°, (b) 30°, and (c) 45°

5 | DAMAGE DETECTION USING PA

5.1 | Wave field in pristine plate

The behavior of the wave field in the pristine plate is first experimentally verified. In particular, the guided wave properties are verified. The center PZT element of the PA is commanded to launch the three-cycle 100-kHz tone-burst signal with a maximum amplitude of 5 V. The identical PZT element in the PA is used to simultaneously record the wave fields received. Due to the plate being in a pristine condition, the PZT element should only observe the initial excitation as reflections of the waves from the plate boundaries that are 45.35 cm from the PZT element in both the x- and y-directions. Figure 9 presents the signal measured by the center PZT element of the PA. The initial excitation is observed although attenuated with a maximum voltage of 1 V. The S_0 and A_0 modes exist in the wave field and reflect from the plate edges at different times based on their different group velocities (Figure 2a).

To assess the time of flight of each mode wave forms, the cross-correlation function, $R_{xy}(\tau)$, is used:

$$R_{xy}(\tau) = \int_{-\infty}^{\infty} x(t) \cdot y(t+\tau) dt, \tag{14}$$

where τ is the time lag between signals $x(t)$ and $y(t)$. The initial excitation signal and the reflected waveforms identified as S_0 and A_0 modes are segmented with the cross-correlation function calculated for varying time lags. The time lag where $R_{xy}(\tau)$ is maximized is considered the time of flight of the mode wave form. Using this method, the times of flight of the S_0 and A_0 modes are determined to be 168 and 420 μs, respectively. Based on the theory of ultrasonic Lamb waves, the group velocities for the S_0 and A_0 mode in a 1.6-mm aluminum plate are 5,465 and 2,172 m/s, respectively. Thus, the traveling
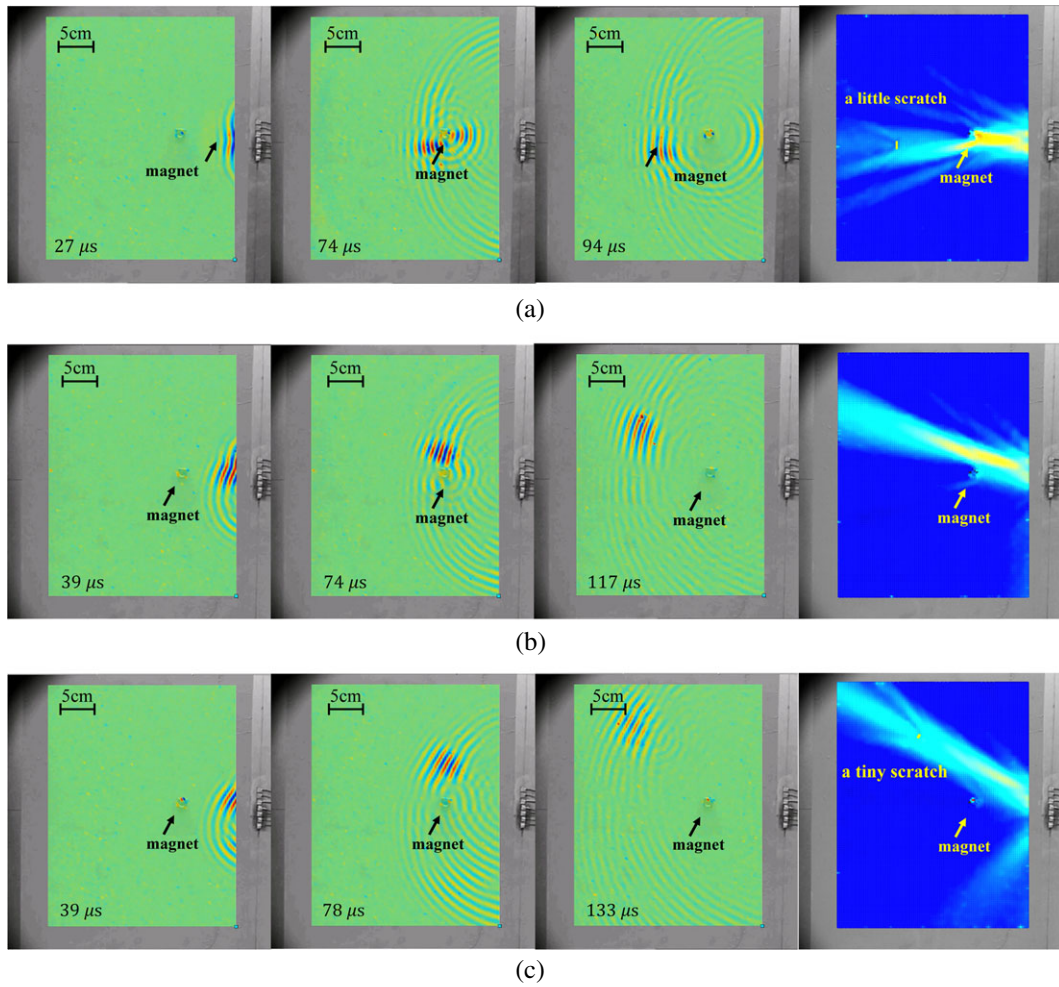
(a)

(b)

(c)

FIGURE 8 Wave field in aluminum plate with surface defect measured by laser Doppler vibrometer when the focal point is $R_F = 10$ cm and at a beam angle, θ_F, of (a) 0°, (b) 30°, and (c) 45°
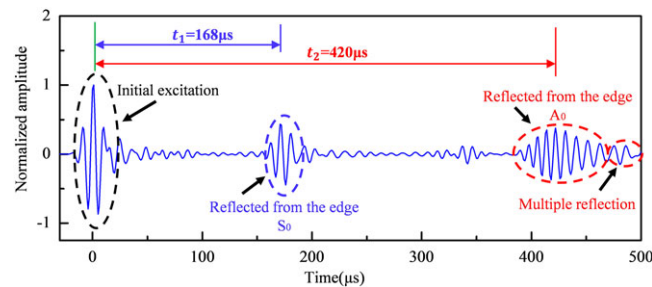

FIGURE 9 Waveform measured by linear phased array in the undamaged aluminum plate with reflected mode travel times calculated by cross-correlation analysis

distance computed using these group velocities are 91.8 and 91.2 cm for the S_0 and A_0 modes, respectively. These two values are within 2% of the travel distance of a round trip between the PA and the edge, which is 90.7 cm based on the measured plate geometry. This verifies the ultrasonic guided waves in the plate behave as theoretically predicted.

5.2 | Influence of damage on wave field

The experiment performed on the pristine plate is repeated but with the magnets placed at $R_d = 10.0$ cm and $\theta_d = 5°$ from the PA. Plotted in Figure 10a is the received signal from the damaged (i.e., magnet mounted) plate superimposed on the
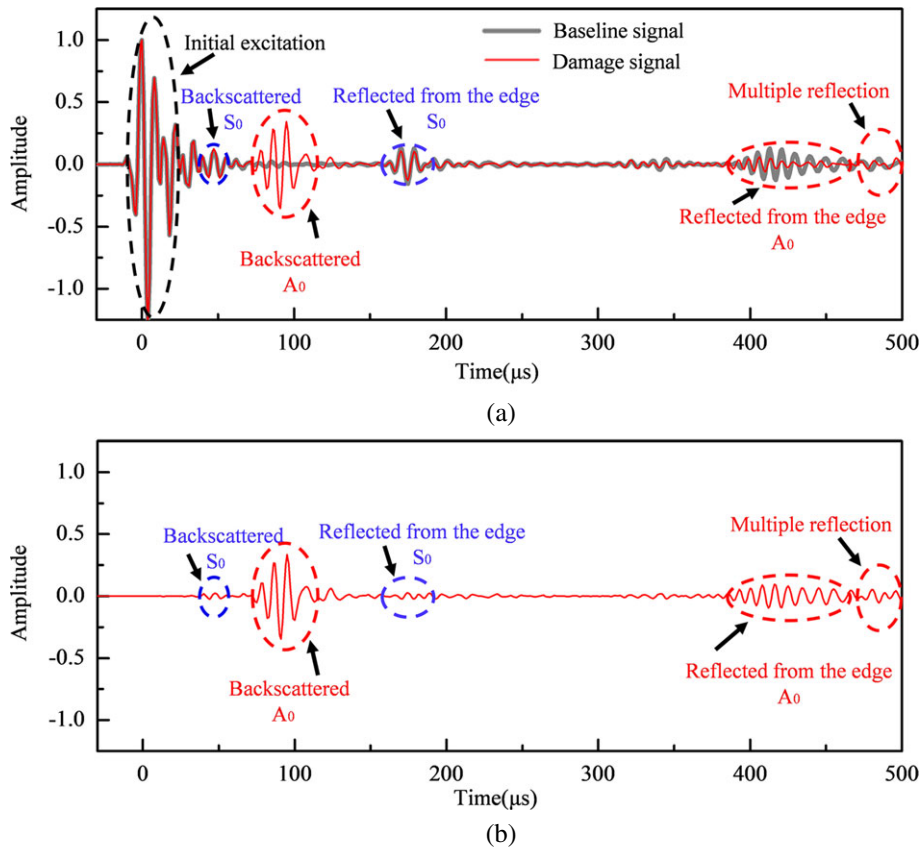
FIGURE 10 (a) Waveform measured by linear phased array in both undamaged (baseline) and damaged (small magnet) aluminum plate; (b) waveform difference between the damaged plate and baseline signals

signal obtained for the same excitation introduced in the pristine plate. Similar to the pristine case, the initial excitation and the reflected S_0 and A_0 modes are evident. However, due to damage, backscattered S_0 and A_0 modes are now present. To better isolate the backscattered modes, the damage signal is subtracted from the pristine (baseline) signal to yield Figure 10b. First, the baseline signal is measured with the structure in the undamaged, pristine state. When evaluating the structure in the damage state, the pristine signal is subtracted from the received signal to yield the difference that can be attributed to damage and not to the complex geometry of the structure. This method yields a more reliable signal for damage assessment in the plate. The energy of the difference signal between the received signal and the pristine signal is plotted at the focal point to derive a color map indicating the strength of echo from damage. Using the group velocities of the S_0 and A_0 modes, the location of the damage relative to the PZT element can be determined from the time of flight of the backscattered wave forms. Two points should be discussed. First, the amplitude of the A_0 mode is larger than that of the S_0 mode; the A_0 mode will therefore be the primary mode used for damage detection using the linear PA. Second, the reflected modes from the edge of the plate are still evident in the difference signal of Figure 10b. This is due to the fact that as the wave field propagates past the damage, it loses energy due to the backscattered signal. As a result, when the reflections are received by the PA, the amplitudes of the reflections are lower compared to the pristine case. This mild level of attenuation results in the reflected signal appearing in the difference signal.

5.3 | Damage detection and localization

To utilize the PA for damage detection, the LabVIEW interface is programmed to scan the plate for damage. Scanning is achieved by methodically changing the focal point distance and angle. Due to the blind spot of the PA caused by the acoustic variations near field to the PA, the PA is configured to scan with focal point radius, R_F, starting at 5 cm and varying in 2.5-cm increments to 25 cm. The PA is also programmed to vary its directional angle, θ_F, from $-90°$ to $90°$ in 15° increments (in spite of there is no limit for the focal degree of the PA) resulting in 117 focal points. For each focal point, the signals received by each element of the PA are collected for the pristine plate to serve as a baseline. When the PA inspects the plate in an unknown state, the baseline signal is subtracted from the signals received by each element of

the array to reveal the backscattered A_0 mode. The cross-correlation method is then used to determine the time lag, δ_m, between the backscattered A_0 modes. For example, consider the case of the magnets placed at $R_d = 10$ cm and $\theta_d = 30°$ relative to the PA. Figure 11 presents the difference signal at each element of the PA when the focal point is set to the damage location. The dotted line in the figure is a curve fit to the estimated time lag, δ_m, between channels. The signals received by the PA are shifted by the time lags and summed to yield the superimposed signal, S_R (Equation 12). The energy of the superimposed signal is the basis for estimating damage in the plate; when damage is present at the focal point, the signal energy of S_R will be large.

The first damage case considered is the magnets placed at $R_d = 10$ cm and $\theta_d = 0°$ as shown in Figure 12a. The PA is commanded to steer the three-cycle 100-kHz tone burst to focus on the 117 focal points with the superimposed signal S_R energy calculated for each focal point. The scan plot of Figure 12b plots the S_R energy over the scan area of the plate with the plot normalized to the largest S_R energy value found. As can be seen, the location of the magnets is easy to identify at the appropriate location. The second damage case adopts a different set of magnets. In this case, larger magnets 3.81 cm by 1.27 cm in area are used. These magnets are attached to the plate at $R_d = 12.5$ cm and $\theta_d = 15°$ as shown in Figure 13a. Similar to the previous case, the location of the magnets is accurately depicted in the scan plot of the S_R energy plotted in Figure 13b. However, the area of elevated S_R energy is larger than in the previous damage case as would be expected due to the larger magnets. These results suggest the PA is capable of detecting, localizing, and sizing damage in the plate.
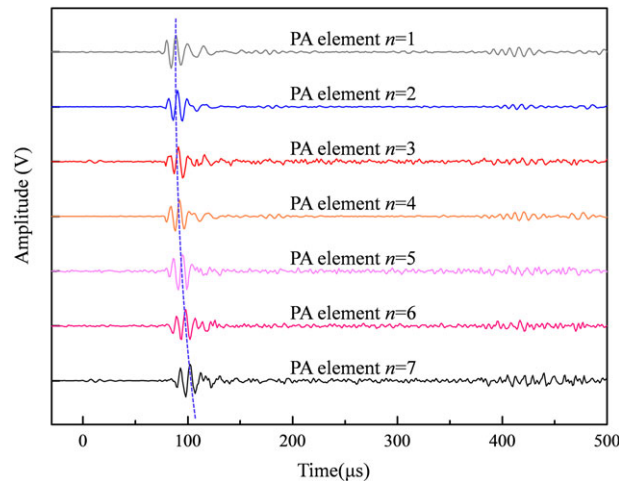

FIGURE 11 Time-synchronized signals received from each element of the phased array (PA) when the focal point is set to the damage location of $R_d = 10$ cm and $\theta_d = 30°$

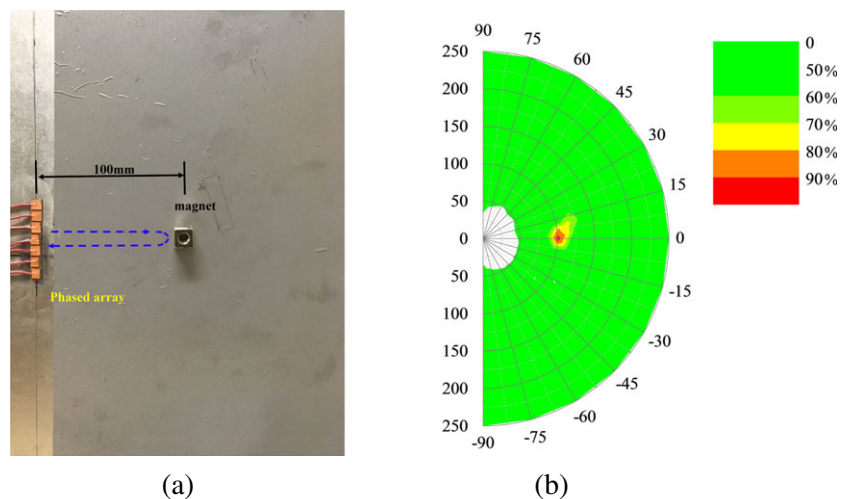**FIGURE 12** (a) Picture of defect (small magnet) applied to the aluminum plate at $R_d = 10$ cm and $\theta_d = 0°$ relative to the linear phased array; (b) scanning map of defect location and size based on superimposed signal, SR, energy
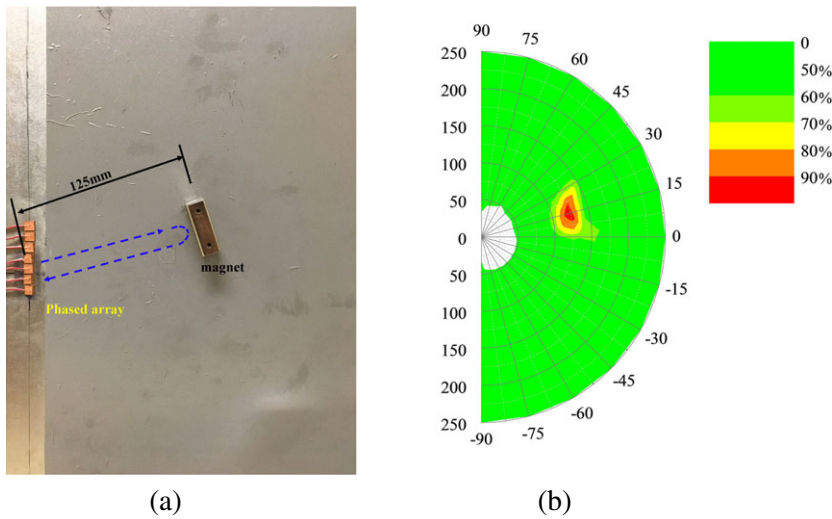
FIGURE 13 (a) Picture of defect (large magnet) applied to the aluminum plate at Rd = 12.5 cm and $\theta_d = 15°$ relative to the linear phased array; (b) scanning map of defect location and size based on superimposed signal, S_R, energy

6 | NUMERICAL SIMULATION

To evaluate the proposed PA methodology for detecting more realistic damage cases, numerical simulation of the thin aluminum plate structure used in the experiment is undertaken. Although many numerical approaches are possible including the finite element method (FEM), this study adopts the LISA.[30] LISA was first developed for ultrasonic guided wave simulation in one-dimensional isotropic structures by Delsanto et al.[31] and later expanded to multidimensional isotropic[32] and anisotropic structures.[33] LISA is derived based on the finite difference method and has proven computationally efficient when parallelized for implementation on graphical processing units. Specifically, accurate simulations using fine meshes can be executed at speeds much faster than what is possible using FEM.[34] A comparison study found that a meshed model with 2 million nodes took more than 10 hr for a commercial FEM software platform (ANSYS) but took LISA less than 30 min with the same mesh size and simulation time.[30,35]

As shown in Figure 14, the original plate that was 91.4 cm by 91.4 cm is now modeled as a smaller 50 cm by 50 cm plate with a 4 cm nonreflective boundary. The adoption of the smaller plate area with a nonreflective boundary conveniently decreases the computational time of the LISA model without altering the realism of the simulation. In the model, the linear PA is placed on the top surface of the plate 5 cm from the plate boundary on one side of the plate. However, a larger number of elements ($N = 16$) are used in the simulation to showcase a more capable PA. The piezoelectric elements are modeled in LISA using classical piezoelectric elements that model the coupled voltage–strain behavior. To model the plate in LISA, the plate is discretized by a rectangular mesh. To ensure accurate results, the mesh discretization should be smaller than at least 10% of the shortest wavelength. For the 1.6-mm-thick 6061 aluminum plate, the wavelengths of the S_0 and A_0 modes for the three-cycle 100-kHz tone burst is determined to be $\lambda_{S_0} = 26.4$ mm and $\lambda_{A_0} = 8.6$ mm, respectively. Based on these wavelengths, the mesh is discretized $\Delta_x = 0.5$ mm, $\Delta_y = 0.5$ mm, and $\Delta_z = 0.2$ mm, where the z-direction corresponds to the axis orthogonal to the plate surface as shown in Figure 14. In a similar fashion, the sampling rate of the simulation should be at least greater than two times the maximum frequency of interest. However, due to the need to satisfy the stability criteria of LISA,[35] a much higher sampling rate is selected; in this study, the time step is set at $\Delta t = 7.0 \times 10^{-8}$ s. Using the theory presented in Section 3, the delay time between PA elements, δ_n, is calculated for each desired focal point (i.e., R_F and θ_F) and implemented in the LISA simulation.

6.1 | Pristine (undamaged) case

The pristine case is simulated to validate the beam steering capabilities of the linear PA. Two cases are simulated with a focal point 20 cm from the PA: $\theta_F = 0°$ and $\theta_F = 30°$. For each case, the delay time for the elements in the linear PA are calculated by Equation 6. Figure 15 provides a graphical depiction of the out-of-plane (z) displacement of the plate at different time points in the simulation. For the first case ($\theta_F = 0°$), the PZT elements of the linear PA fires sequentially with the wave fronts mixing. As the wave field propagates, the beam width becomes narrower and finally converges on the focal point at 126 μs. At that point, the z-direction displacement is larger than the wave fields shown prior at 42 and 84 μs. After converging on the focal point, the wave begins to spread out and reduces in amplitude
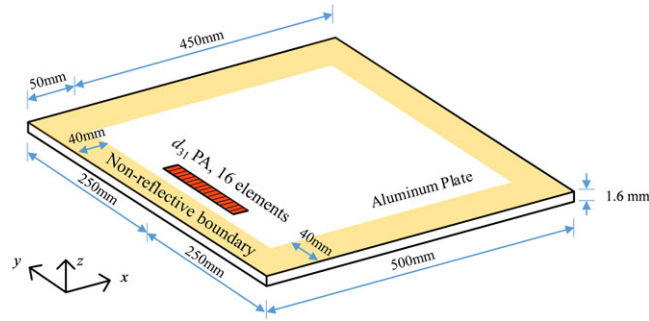
FIGURE 14 Layout of linear phased array (PA) system on aluminum plate

(as is evident at 210 μs). Figure 15b presents a time-lapsed depiction of the waveform for the second case. Again, the linear PA generates a series of waveforms that begin to radiate along $\theta_F = 30°$. As the waveform radiates outward from the PA, it converges on $R_F = 20$ cm. At 160 μs, maximum convergence occurs at the focal point with the greatest z-direction amplitude of the plate achieved. After converging, the waveform spreads out as shown for the plate displacement at 250 μs. In a real plate, the wave fields shown in Figure 15 would also have a symmetric counterpart radiating to the left of the linear PA. None the less, the result depicted in Figure 15 demonstrates that the PA can steer the ultrasonic wave field with great ease.

6.2 | Damaged case

To simulate realistic damage in a plate, a thin notch roughly 1 cm long and 1 mm wide is introduced to simulate a fatigue crack. The notch is parallel to the y-axis of the plate, and its center is placed at $R_d = 20.0$ cm and $\theta_d = 30°$ relative to the PA. In the model, the notch penetrates through the thickness of the plate. In the simulation, the focal point of the linear PA is selected to be at the same location of the damage (i.e., $R_F = R_d$ and $\theta_F = \theta_d$). The displacement of the plate in the z-direction is plotted in Figure 16 for four instances in time: 55, 105, 160, and 270 μs. As can be observed in the figure, the wave field generated by the linear PA focuses at 160 μs on the damage location. Compared with the wave field in the pristine case (Figure 15b), the concentrated wave field at the focal point interacts with the damage located at this point. Due to the existence of the notch, a major portion of the incident wave field is backscattered by the damage whereas a smaller portion of the original wave field radiates past the damage site. The backscattered wave field radiates back to the PA where it can be measured and analyzed. The LISA model provides a basis for modeling and analyzing how the active PA can be used to detect, locate, and size damage in metallic plate structures.
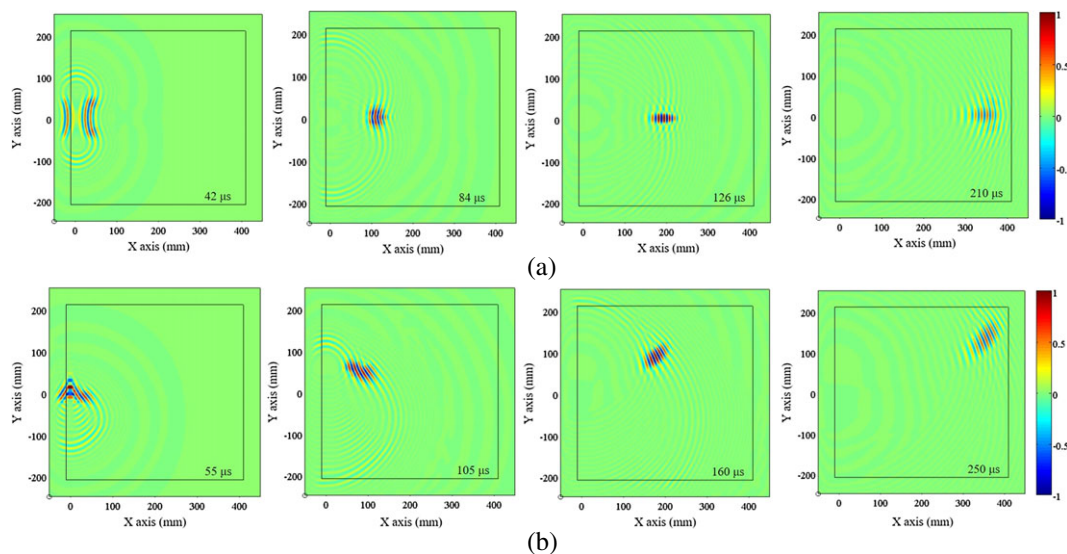

FIGURE 15 Simulation results (z-direction displacement in mm) of the linear phased array of 16 PZTs focusing on 20 cm: (a) 0° and (b) 30°

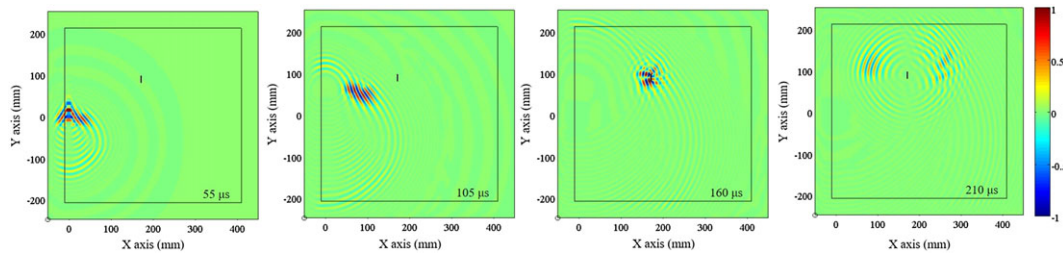**FIGURE 16** Simulation results (z-direction displacement in mm) of the linear phased array of 16 PZTs focusing on 20 cm and 30° with a notch present

7 | CONCLUSIONS

In the paper, a true time-delay ultrasonic PA using a traditional National Instruments data acquisition system was proposed for damage detection in metallic plate structures. Unlike previous work in piezoelectric element-based PA, which use postprocessing to focus the wave, the proposed method used preprocessing to physically steer a wave to focus on a specific point on the plate. In doing so, a strong backscattered signal can be received by the PA defined by a high SNR from which accurate data detection is achieved. The work is highly novel because it experimentally integrated guided wave methods within a standard SHM data acquisition platform widely used in the field. To further highlight the benefits of adopting a traditional data acquisition platform, an LDV was also integrated with the National Instruments system to time synchronize the collection of out-of-plane wave fields generated by the PA. Using the PA to scan a circular area around the PA, damage in the form of magnets mounted to the plate surface were accurately identified in terms of their location and size. Finally, the work also adopted the LISA simulation environment to accurately simulate the behavior of a linear PA in isotropic metallic plates for a damage case related to fatigue cracks.

Although this paper presented results that indicate the effectiveness of a true time delay PA, the study only focused on the case of a single damage event in the plate. Future work is needed to explore the damage detection capabilities of the PA approach when multiple damage events are present, especially in high attenuative media (e.g., composites). Furthermore, more realistic damage cases should be considered including the ability of a PA to identify fatigue cracks and loss of section due to corrosion in the plate. One drawback of the linear PA design is that it cannot identify if the damage event is in front or behind the PA; hence, future work should also explore 2D arrays as a means of providing unequivocal damage localization relative to the PA. Finally, the PA strategy could be improved by implementing an adaptive beam steering methodology that more finely scans a structure around areas suspected of having damage based on a preliminary, coarser scan.

ORCID

Wentao Wang http://orcid.org/0000-0003-1811-1748
Jerome P. Lynch http://orcid.org/0000-0002-8793-0061

REFERENCES

[1] P. C. Chang, A. Flatau, S. Liu, *Struct. Health Monitoring* **2003**, *2*, 257.

[2] S. W. Doebling, C. R. Farrar, M. B. Prime, D. W. Shevitz, Damage identification and health monitoring of structural and mechanical systems from changes in their vibration characteristics: A literature review. **1996**, LA-13070-MS.

[3] C. R. Farrar, K. Worden, *Philosophical Trans. Royal Soc. London A: Mathematical Phys. Eng. Sci.* **2007**, *365*, 303.

[4] J. P. Lynch, K. J. Loh, *Shock and Vibration Digest.* **2006**, *38*, 91.

[5] S. S. Kessler. **2002**, Piezoelectric-based in-situ damage detection of composite materials for structural health monitoring systems. Massachusetts Institute of Technology.

[6] A. Raghavan, C. E. Cesnik, *Shock and Vibration Digest.* **2007**, *39*, 91.

[7] Y. Lu, L. Ye, Z. Su, C. Yang, *Ndt & E Int.* **2008**, *41*, 59.

[8] H. Sohn, H. W. Park, K. H. Law, C. R. Farrar, *J. Aerospace Eng.* **2007**, *20*, 141.

[9] Z. Su, L. Ye, Y. Lu, *J. Sound Vib.* **2006**, *295*, 753.

[10] K. Diamanti, C. Soutis, J. Hodgkinson, *Composites Part A: Appl. Sci. Manufact.* **2005**, *36*, 189.

[11] J. L. Rose, Y. Cho, M. J. Avioli, *J. Loss Prevention Process Indust.* **2009**, *22*, 1010.

[12] J. L. Rose, *Ultrasonic waves in solid media*, Cambridge university press, Cambridge, UK **2004**.

[13] Y. Shen, V. Giurgiutiu, *Struct. Health Monitoring* **2014**, *13*, 1.

[14] V. Giurgiutiu, *J. Intell. Mater. Syst. Struct.* **2005**, *16*, 291.

[15] A. Raghavan, C. E. Cesnik, *Smart Mater. Struct.* **2005**, *14*, 1448.

[16] V. Giurgiutiu, *Structural health monitoring: With piezoelectric wafer active sensors*, Academic Press, Cambridge, Massachusetts, US **2007**.

[17] H. Sohn, S. J. Lee, *Smart Mater. Struct.* **2009**, *19*, 1.

[18] F. Yan, R. L. Royer, J. L. Rose, *J. Intell. Mater. Syst. Struct.* **2010**, *21*, 377.

[19] W. Zhou, H. Li, F.-G. Yuan, *Smart Mater. Struct.* **2013**, *23*, 1.

[20] C. Zhou, Z. Su, L. Cheng, *Mech. Syst. Signal Process.* **2011**, *25*, 2135.

[21] S. Pierce, B. Culshaw, W. Philp, F. Lecuyer, R. Farlow, *Ultrasonics* **1997**, *35*, 105.

[22] R. C. Hansen, *Phased array antennas*, John Wiley & Sons, **2009**.

[23] L. W. Schmmer Jr, *Mod. Phys. Lett. B* **2008**, *22*, 917.

[24] L. Yu, V. Giurgiutiu, *J. Mech. Materials Struct.* **2007**, *2*, 459.

[25] J. L. Rose, *SPIE Smart Struct. Materials+ Nondestructive Eval. Health Monitoring*, **2011**. https://doi.org/10.1117/2.4201601.23.

[26] P. Wilcox, D. O. Thompson, D. E. Chimenti, C. Nessa, S. Kallsen, L. Poore, *AIP Conf. Proc.* **2003**, https://doi.org/10.1117/2.4201601.23.

[27] P. M. Monje, L. Casado, G. Aranguren, V. Cokonaj, E. Barrera, M. Ruiz, *Eur. Workshop Struct. Health Monitoring* **2012**.

[28] M. Mitra, S. Gopalakrishnan, *Smart Mater. Struct.* **2016**, *25*, 053001.

[29] L. W. Schmerr, *Fundamentals of ultrasonic phased arrays*, Springer **2014**.

[30] H. Zhang, C. E. Cesnik, *SPIE Smart Struct. Materials+ Nondestruct. Eval. Health Monitoring* **2016**.

[31] P. Delsanto, T. Whitcombe, H. Chaskelis, R. Mignogna, *Wave Motion* **1992**, *16*, 65.

[32] P. Delsanto, R. Schechter, H. Chaskelis, R. Mignogna, R. Kline, *Wave Motion.* **1994**, *20*, 295.

[33] Y. Shen, C. E. Cesnik, *Smart Mater. Struct.* **2016**, *25*, 1.

[34] P. Delsanto, R. Schechter, R. Mignogna, *Wave Motion.* **1997**, *26*, 329.

[35] K. S. Nadella, C. E. Cesnik, *SPIE Smart Struct. Materials+ Nondestructive Eval. Health Monitoring*, **2012**.